MISS VANESA BARBERON (Orcid ID : 0000-0002-3186-8289)

Article type : Paper

Received date: 25-Sept-2017

Revised version received date: 16-Apr-2018

Accepted date: 02-May-2018

Late Cenozoic brittle deformation in the Southern Patagonian Andes: record of plate coupling/decoupling during variable subduction?

Vanesa Barberón[1*]; Christian Sue[2]; Matías Ghiglione[1]; Gonzalo Ronda[1] and Eugenio Aragón[3,4]

(1) IDEAN (Universidad de Buenos Aires-CONICET), Buenos Aires, Argentina.

** email: vanesabarberon@yahoo.com.ar*

(2) Franche-Comté University Besançon, CNRS-UMR6249, OSU-THETA, France.

(3) Centro de Investigaciones Geológicas (UNLP-CONICET), 1 Nº 644, (1900) La Plata, Buenos Aires, Argentina.

(4) Facultad de Ciencias Naturales y Museo, Universidad Nacional de la Plata, 122 y 60, s/n. (1900), La Plata, Buenos Aires, Argentina.

This article has been accepted for publication and undergone full peer review but has not been through the copyediting, typesetting, pagination and proofreading process, which may lead to differences between this version and the Version of Record. Please cite this article as doi: 10.1111/ter.12339

Correspondence details:

Miss Vanesa Barberon

Facultad de Ciencias Exactas y Naturales

Universidad de Buenos Aires

Buenos Aires

Argentina

Tel: (+54 +11) 4576-3400

Abstract

The Andes of southern Patagonia experienced a Miocene shift towards faster and higher angle subduction followed by the approach and collision of the Chile oceanic ridge. We present a kinematic study characterizing palaeostress fields computed from brittle tectonics, to better constrain upper-crustal deformation during this complex scenario. Although previous studies already suggested variable kinematics, it is striking that in a long-lasting subduction environment, the computed palaeostress tensors are mostly strike-slip (55%), while 35% are extensional, and only 10% compressive, concentrated along a main frontal thrust. Cross-cutting relationships and synsedimentary deformation indicates that a long-lived strike-slip regime was punctuated by a lower Miocene extensional event in the foreland before the main compressional event. The results are discussed in contrasting geodynamic models of plate coupling/decoupling *vs.* direction and rate of convergence of the subducting plate, to explain the main mechanisms that control back-arc deformation.

Keywords: *Southern Andes; Patagonia; brittle deformation; geodynamics; tectonics; plate coupling/decoupling*

1. Introduction

Evolution of Neogene deformation in the Southern Patagonian Andes (SPA) was related to changes in convergence vectors and to subduction of the Chile oceanic ridge (COR; Bourgois *et al*., 2000; Somoza and Ghidella 2005, 2012; Ghiglione and Cristallini 2007; Scalabrino *et al*., 2010). During an early Miocene plate reorganization event (~23 Ma; Lonsdale, 2005), oblique subduction towards southern South America shifted from subduction of the Farallon plate (NE ~5 cm/yr) to the faster and higher-angle Nazca plate (ENE ~15 cm/yr) (Somoza and Ghidella 2005, 2012). This event was followed by collision of segments of COR since ~15 Ma, generating contrasting scenarios of subduction north and south of the Chile triple junction (CTJ).

Oblique subduction of the fast and oblique Nazca plate (az. 10° 8 cm/yr; Gripp and Gordon, 1990; DeMets *et al*., 1990) north of the CTJ presently produces partitioning of deformation along the Liquiñe-Ofqui dextral strike-slip system (Fig. 1a; Hervé, 1994), while south of the CTJ, subduction of the slower Antarctic plate (NE 2 cm/yr) generates almost no upper-plate-related deformation (Scalabrino *et al*., 2010). The CTJ has moved northward from ~55° to its present position at ~46° during the Miocene (*e.g*. Cande and Leslie, 1986; Scalabrino *et al*., 2011; Aragón *et al.,* 2013), and our working hypothesis is that the boundary separating these two contrasting deformation domains has moved accordingly. Therefore, strike-slip deformation could dominate in the SPA, which has undergone a long period of oblique subduction previous to collision of ridge segments (Fig. 1b–d).

In order to characterize and understand the stress field along the foothills of the SPA we present 54 new palaeostress tensors, obtained at 48 sites (Fig. 2a). We established a succession of the three end-member tectonic regimes in a quite short period of time. Analysis of cross-cutting relations and synsedimentary deformation indicates that long

lasting transcurrent deformation was interrupted by a prompt extensional event coeval with the early Miocene plate reorganization, followed by the compressional event producing basement thrusting. Our results show that back-arc deformation is strongly affected by oceanic plate reorganization in the subduction zone, and can lead to fundamental contrasts in terms of tectonic and sedimentary events.

2. Geological and tectonic setting

The Late Cenozoic evolution of the SPA is one of the most prominent examples of coupling between subduction dynamics, climate and tectonic deformation (Lagabrielle *et al*., 2009). Existing thermochronological data (Thomson *et al.*, 2001, 2010; Fosdick *et al.*, 2013; Guillaume *et al.*, 2013) indicate enhanced exhumation that migrated eastward between ~33 Ma and 5–3 Ma, potentially related to the approach and collision of the COR (Haschke *et al.*, 2006; Scalabrino *et al*., 2011). For the northern SPA a Miocene pre-ridge dextral transpressional deformation due to fast oblique subduction has been proposed (Scalabrino *et al*., 2009), followed by late Miocene–Pliocene compression during ridge collision and a post-ridge extensional stage concomitant with glaciations at the latitude of the present CTJ (Lagabrielle *et al*., 2004; 2007). However, kinematic data necessary to understand the complex space and time pattern of deformation are still scarce at a more detailed regional scale, the nature and kinematics of faulting being still open to discussion.

The studied sector is subdivided by the Basement thrust, a segmented fault with east vergence and ~N–S orientation (Fig. 2a), which superposes Jurassic–Cretaceous and Late Cenozoic rocks over the Miocene units (Giacosa and Franchi, 2001). The basement front segment delimited by the Sierra Colorada Fault is shifted towards the east relative to the regional trend (Figs. 2a,b and 3a), a characteristic that can be related to the tectonic inversion of Mesozoic rift structures in the foreland (Giacosa and Franchi, 2001; Sruoga *et*

al., 2014), as shown also in the southern end of the SPA (Likerman *et al.,* 2013; Ghiglione *et al.,* 2014). The structural domain located to the west of the Basement thrust is characterized by NNW-oriented fold-and-thrust sheets involving Palaeozoic basement with ductile deformation, Jurassic synrift volcanics and Cretaceous retroarc sequences (Giacosa and Franchi, 2001; Ghiglione *et al.,* 2015, 2016). The external domain placed to the east is composed of Mio-Pliocene and some scattered Cretaceous units, which form a frontal monocline (Fig. 2).

3. Brittle deformation analysis

We used field observations and mapping work at different scales, ranging from satellite images (Fig. 3a) to meso-scale field observations and measurements (Figs. 4, 5a and 6). At a regional scale, satellite image analysis (Landsat TM, ALOS-PALSAR) west of Sierra Colorada fault led to the mapping of kilometric-scale lineaments in the El Quemado Complex (Jurassic volcanics) (Fig. 3a). Analysis of lineament directions shows 3 main families, a dominant N–S-oriented set, and secondary W–NW, and E–NE families (Fig. 3b). The comparison with directional statistics of the meso-scale faults measured in the same area reveals a good correlation (Fig. 3b). Indeed, the N–S-trending set and E–NE fault directions are recognized. The comparison between faults and lineament distributions at complementary scales confirms that meso-scale faults are representative of the distribution of regional brittle deformation (Ghiglione 2002; Rosenau *et al*. 2006).

The established directional distribution overall fits well with a regional N–S right-lateral Riedel fault system (Fig. 3c; Riedel, 1929) parallel to the front of the orogen, as shown by well represented N–S-trending main M dextral faults and N–NE-trending R dextral faults (Fig. 3d). E–NE-trending R' left-lateral faults, and N–NW trending P dextral faults show

some scattering but also have a reasonably good fit (Fig. 3d). The N–NE families of reverse faults and N–NW extensional faults can be related, respectively, to the compressional and extensional events described below.

Beyond this specific mapping justified by the exceptional exposure of large-scale brittle structures in the El Quemado Complex, we systematically collected minor fault data (Figs. 4 and 5a) along the frontal region of the SPA, to determine the related palaeostress orientations.

In terms of methodology, fault/striae analysis is based on the Wallace and Bott principle (Wallace, 1951; Bott, 1959), which has long been discussed and still remains a matter of debate concerning stress *vs.* strain relationships (e.g. Angelier and Mechler, 1977; Twiss and Unruh, 1998; Yamaji, 2000). This principle states that faults slip parallel to the direction of maximum resolved shear stress on the considered plane of the local spatially homogeneous stress tensor (refer to Lacombe, 2012; Riller *et al*., 2017 for further discussion).

About 1000 fault planes and their slickensides were measured at 48 sites, from which 54 palaeostress tensors were calculated, including their principal stress orientations and the related Φ-ratio ($\Phi = (\sigma 2 - \sigma 3)/(\sigma 1 - \sigma 3)$) representing the shape of the stress ellipsoid (see Table 1 with detailed parameters and the stereonet plate provided in supplementary material). In six sites, superimposed brittle deformation stages could be differentiated from cross-cutting relationships, leading to two palaeostress tensor inversions (Table 1). The MIM© software was used in order to determine the stress axes (Yamaji *et al.,* 2011). The stability and the quality (Q parameter) of each tensor were estimated from a series of

criteria, including the visualization of the inverse function (Yamaji, 2000), the distribution of the measurements, the number of faults used in the inversion, the average misfit angle M and a geometrical coherency test using the geometric right-dihedra method (Angelier and Mechler, 1977) and PBT method (Delvaux, 1993).

Tensor's qualities were classified from 1 (very good) to 3 (low quality), and only about 15% of the measurements have been discarded due to the high misfit individual angle. About 13 tensors exhibit plunge of sub-horizontal axes above 15°, and only 2 above 20°, and/or plunges of sub-vertical axes lower than 70°, and could be back-tilted according to S_0 (palaeo-horizontal) following the andersonian theory. These tensors were rotated to test changes in stress orientation, but only number 48 presented noticeable changes and reasonable field arguments showing its tilting (Figs. 5b,c; see discussion below). Accordingly, only tensor 48 was kept rotated in the final database.

The overall stress map (Fig. 7) includes comparable strain axes; shortening and stretching directions published by Diraison *et al.* (2000) and Lagabrielle *et al.* (2004). The obtained stress field is quite complex, and presents the three main deformational modes (extension, compression, strike-slip). Looking at the strike-slip tensors (about 55% of the total) two major directions arise from our database (Fig. 7), with subhorizontal σ_1 at az. ~30º and ~110º, associated to subhorizontal σ_3 axis at az. ~120º and ~20º, respectively. Extensional tensors represent 35% of our database with corresponding best σ_3 axis oriented at az. ~60° (dominant direction) and az. ~150° (minor direction). A minority of reverse tensors (10%) arise with a best σ_1 axis oriented at az. ~45°.

The Φ-ratio (shape of the stress ellipsoid; Fig. 8), constrains the mode of deformation prevailing during the brittle phase(s) (Ritz and Taboada, 1993; Tricart *et al*., 2006; Beucher *et al*., 2017). The transcurrent tensors (31 data) show a clear unimodal distribution, with one central peak at around 0.5, which indicates a pure strike-slip system. On the contrary, a bimodal distribution for the 19 extensional tensors, with a main peak at low values (0.2) indicates a multi-trend extension, and a second peak around 0.7, indicating a tendency to transtension (Fig. 8). The 4 reverse tensors do not allow providing reliable statistics.

4. Discussion and conclusions

Through the determination of palaeostress tensors our results show the existence of the three main modes of deformation in the SPA (Fig. 7), distributed as follows: strike-slip deformation prevails in the western basement domain, while extension was observed in the lower Miocene foothills (Figs. 5a and 6) underneath the compression-dominated Basement thrust front (Fig. 2b). How such a particular pattern of deformation may arise from the regional geodynamics, and in which temporal order, are the main concerns of this discussion.

Several authors have proposed a transpressional regime for the SPA based on the measurement of widespread strike-slip kinematic indicators (Coutand *et al.,* 1999; Diraison *et al.* 2000; Lagabrielle *et al.* 2004). The Eocene–Miocene scenario with oblique convergence of the Farallon and Nazca plates (Figs. 1b–d; Cande and Leslie, 1986) seems to be responsible for the transcurrent scenario (*i.e.* Scalabrino et al., 2010) and widespread strike-slip deformation of the basement domain (Fig. 7), which is comparable to the current dynamics of the Northern Patagonian Andes (Fig. 1a; Cembrano and Hervé, 1993; Rosenau *et al*. 2006; Georgieva *et al.* 2016). We suggest that overall Neogene deformation may have been dominated by transpressional right-lateral deformation partitioning along the Basement

thrust (Fig. 1 c,d), *i.e.* a now extinct ancestor of the Liquiñe-Ofqui fault. For the particular case of the Sierra Colorada fault segment, an origin during Jurassic extensional/trantensional deformation has been proposed (Sruoga *et al.,* 2014), *i.e.* providing a weakness zone readily reactivated during oblique subduction and related partition of deformation. Subordinate and scattered extensional deformation is affecting the Basement domain (Fig. 7), interpreted as relicts from the Jurassic rift. The results are overall in accordance with expected transcurrent deformation dominating the SPA during oblique subduction previous to collision of ridge segments (Fig. 1b,c).

Lagabrielle et al. (2004) recognized synsedimentary folds and thrusts in the lower part of the Río Zeballos Group (Río Jeinemeni Formation; lower Miocene) along superb exposures in the Jeinemeni river southern cliff, and proposed a major contractional/transpressional? phase leading to the development of the main Basement thrust (Fig. 2a). New exposures at the base of the cliff reveal an extensional phase underlying the thrusting event (Fig. 6). Another example of this event of synextensional deformation can be found in the Lincoln river area (Fig. 5a). We documented outcrops of extensional growth strata and grabens that are overlain by the main thrust affecting Jurassic to Miocene sequences, and include rotated normal faults in the Río Jeinemeni Formation. Once back-tilted, these faults provided an extensional tensor (#48 Fig. 5b; see discussion above). This outcrop illustrates the synsedimentary nature of the deformation, indicated by depositional sequences thickening towards the listric faults and a decrease in dip from older to younger strata (Fig. 5a), a fact that allows us to state that the extensional phase took place during deposition of the growth strata in the early Miocene (Fig. 5c). Another indication constraining the age of extensional faulting is that the synrift formations are sealed by a horizontal post-extensional sequence made of undeformed strata from the Cerro Boleadoras Formation (Figs. 5c and 6). In concordance, many other tensors calculated in subhorizontal Miocene outcrops located at the latitude of the Buenos Aires plateau to the east of the

Basement thrust, *i.e.* not affected by later compression, yielded extensional palaeostress axes (Fig. 7), therefore reflecting their syn-extensional nature.

Afterwards, the COR moved towards the South American margin, triggering the compressional thrusting of the Basement front (Lagabrielle *et al.*, 2004). Tensors along the main thrust front between Lincoln River and Paso Roballos confirm its compressional nature (Figs. 5b and 7). Synsedimentary folds and thrusts cropping out along Jeinemeni river's southern cliff (Lagabrielle *et al*., 2004), and covering the synrift sequences (Fig. 6), give an indication of the sudden passage from extension to compression. These sequences are covered by the post-deformational Cerro Boleadoras Formation, constraining the short time-lapse in which synrift deposition was followed by the Basement thrusting phase (Fig. 5c). The geodynamic setting during the middle Miocene included young and hot approaching oceanic crust from the COR (Fig. 1c), *i.e.* positive buoyancy slab and shallower subduction angle, indicating a possible episode of enhanced coupling between the South America and Nazca plates. A tenfold acceleration in sedimentation rates (~100 m/My) calculated for the 18–14 Ma period (Blisniuk *et al*., 2005) strengthens the interpretation of high coupling between the plates (see Horton and Fuentes, 2016; Horton, 2018).

In summary, the brittle deformation recorded in the SPA shows general strike-slip predominance in the Basement domain, probably due to deformation partitioning along the Basement thrust during Neogene oblique subduction. Evidence of synsedimentary normal faulting in lower Miocene rocks reflects an extensional palaeostress field coeval with low sedimentation rates, which could have taken place during an early Miocene event of plate decoupling. Afterwards, the SPA underwent a Middle Miocene compressional phase together with a tenfold increase in sedimentation driven by plate coupling, a consequence of the approach and collision of hot and young oceanic crust.

Acknowledgements

This work was carried out thanks to the financial support of grants projects Agencia PICT-2013-1291; CONICET PIP 2014-2016 GI directed by M.G., Argentinian-French ECOS-SUD project A15U02 (CS, and MG), and thanks to the French projects Franco-Suisse (Franche-Comté region), and SYSTER (INSU CNRS) directed by C.S. The authors are grateful to Parques Nacionales of Argentina for permitting access to *Perito Moreno* and *Patagonia National Parks*. Special thanks to the park rangers at Lago Belgrano, *Comisión de Fomento* de Hipólito Yrigoyen, and the people of Lago Posadas, especially to Luciana and Gendarmería for allowing access to outcrops, kind logistical support and assistance. This is contribution R-223 of the Instituto de Estudios Andinos IDEAN Don Pablo Groeber (UBA-CONICET).

References

Angelier, J., and Mechler, P., 1977. Sur une methode graphique de recherche des contraintes principales egalment utilisable en tectonique et en seismologie: La methode des diedres droits. Bulletin de Societie Geologique de France, 19,1309-1318.

Aragón, E., Pinotti, L., Fernando, D., Castro, A., Rabbia, O., Coniglio, J., Demartis, M., Hernando, I., Cavarozzi, C.E. and Aguilera, Y.E., 2013. The Farallon-Aluk ridge collision with South America: Implications for the geochemical changes of slab window magmas from fore-to back-arc.Geoscience Frontiers, 4(4), 377-388.

Beucher, R., Sue, C. and Tricart, P., 2017. Orogen-parallel brittle extension as a major tectonic imprint in the Neogene evolution of the south-western Alpine arc. Int J Earth Sci (Geol Rundsch), 106: 2973. Doi :10.1007/s00531-017-1476-7

Blisniuk, P. M., Stern, L. A., Chamberlain, C. P., Idleman, B., & Zeitler, P. K. (2005). Climatic and ecologic changes during Miocene surface uplift in the Southern Patagonian Andes. Earth and Planetary Science Letters, 230(1), 125-142.

Bott, M.H., 1959. The mechanism of oblique slip faulting. Geol. Mag. 96, 109–117.

Bourgois, J., Guivel, C., Lagabrielle, Y., Calmus, T., Boulègue, J., and Daux, V., 2000. Glacial-interglacial trench supply variation, spreading-ridge subduction, and feedback controls on the Andean margin development at theChile triple junction area (45-48° S). Journal of Geophysical Research, 105:8355-8386.

Cande, S. C., and Leslie, R. B., 1986. Late Cenozoic tectonics of the southern Chile trench. Journal of Geophysical Research-Solid Earth and Planets, 91(B1), 471-496, doi: 10.1029/JB091iB01p00471

Cembrano, J. and Hervé, F, 1993. The Liquine Ofqui fault zone: a major cenozoic strike slip duplex in the Southern Andes, paper presented at ISAG, ORSTOM Editions, Paris, Oxford, U.K.

Coutand, I., Diraison, M., Cobbold P. R., Gapais, D., Rossello, E. A. and Miller, M., 1999. Structure and kinematics of a foothills transect, Lago Viedma, southern Andes (49º30S), J. South Am. Earth Sci., 12, 1- 15.

DeMets, C., Gordon, R. G., Argus, D. F., and Stein, S., 1990. Current plate motions. Geophysical journal international, 101(2), 425-478.

Delvaux, D., 1993. The TENSOR program for reconstruction: examples from the East African and the Baikal rift zones.Terra Abstracts. Abstract Supplement, 1 to Terra Nova, 5: 216.

Diraison, M., Cobbold, P.R., Gapais, D., Rossello, E.A. and Le Corre, C., 2000. Cenozoic crustal thickening, wrenching and rifting in the foothills of the southermost Andes. Tectonophysics, 316, 91-119.

Eagles, G. and Jokat, W., 2014. Tectonic reconstructions for paleobathymetry in Drake Passage. Tectonophysics, 611, 28-50.

Escosteguy, L., Dal Molín, C., Franchi, M., Geuna, S., Lapido, O. and Genini, A., 2003. Hoja Geológica 4772-II, Lago Buenos Aires. Provincia de Santa Cruz. Instituto de Geología y Recursos Minerales, Servicio Geológico Minero Argentino. Boletín 339, 80 p., Buenos Aires.

Fosdick J.C., Grove M., Hourigan J.K. and Calderón M., 2013. Retroarc deformation and exhumation near the end of the Andes, southern Patagonia. Earth Planet Sc Lett 361:504–517

Georgieva, V. , Melnick, D., Schildgen, T. F., Ehlers, T. A., Lagabrielle, Y, Enkelmann, E. and Strecker, M. R., 2016. Tectonic control on rock uplift, exhumation and topography above an oceanic-ridge collision – Southern Patagonian Andes (47°S), Chile. Tectonics. doi: 10.1002/2016TC004120

Gephart, J.W., 1990. FMSI: A Fortran program for inverting fault/slickenside and earthquake focal mechanism data to obtain the regional stress tensor. Comput. Geosci. 16, 953–989.

Ghiglione, M. C., 2002. Diques clásticos asociados a deformación transcurrente en depósitos sinorogénicos del Mioceno inferior de la Cuenca Austral. Revista de la Asociación Geológica Argentina, 57(2), 103-118.

Ghiglione, M. C., and Cristallini, E. O., 2007. Have the southernmost Andes been curved since Late Cretaceous time? An analog test for the Patagonian Orocline. Geology, 35(1), 13-16.

Ghiglione, M. C., Ramos, V. A., and Cristallini, E. O., 2010. Fueguian Andes foreland fold and thrust belt: structure and growth strata. Andean Geology, 29(1), 17-41.

Ghiglione, M. C., Likerman, J., Barberón, V., Beatriz Giambiagi, L., Aguirre-Urreta, B. and Suarez, F., 2014. Geodynamic context for the deposition of coarse- grained deep- water axial channel systems in the Patagonian Andes. Basin Research, 26(6), 726-745.

Ghiglione, M. C., Naipauer, M., Sue, C., Barberón, V., Valencia, V., Aguirre-Urreta, B. and Ramos, V. A., 2015. U–Pb zircon ages from the northern Austral basin and their correlation with the Early Cretaceous exhumation and volcanism of Patagonia. Cretaceous Research, 55, 116-128.

Ghiglione, M.C., Ramos, V., Cuitiño, J., and Barberón, V., 2016. Growth of the Southern Patagonian Andes (46 -53°S) and its relation with subduction processes. In “Growth of the Southern Andes” Springer Earth System Sciences, 201-240.

Giacosa, R. and Franchi, M., 2001. Hojas Geológicas 4772-III y 4772-IV Lago Belgrano y Lago Posadas, provincia de Santa Cruz. Servicio Geológico Minero Argentino, Boletín, 256.

Gripp, A. E., and Gordon, R. G., 1990. Current plate velocities relative to the hotspots incorporating the NUVEL- 1 global plate motion model. Geophysical Research Letters, 17(8), 1109-1112.

Guillaume, B., Gautheron, C., Simon-Labric, T., Martinod, J., Roddaz, M. and Douville, E., 2013. Dynamic topography control on Patagonian relief evolution as inferred from low temperature thermochronology. Earth Planet. Sci. Lett., 364, 157–167.

Haschke, M., Sobel, E. R., Blisniuk, P., Strecker, M. R. and Warkus, F., 2006. Continental response to active ridge subduction. Geophysical research letters, 33(15).

Hervé, F., 1994. The southern Andes between 39 and 44 S latitude: the geological signature of a transpressive tectonic regime related to a magmatic arc. In Tectonics of the Southern Central Andes (pp. 243-248). Springer Berlin Heidelberg.

Horton, B. K., and Fuentes, F., 2016. Sedimentary record of plate coupling and decoupling during growth of the Andes. Geology, 44(8), 647-650.

Horton, B. K. (2018). Sedimentary record of Andean mountain building. Earth-Science Reviews. v. 178, p. 279-309, doi.org/10.1016/j.earscirev.2017.11.025.

Lacombe, O., 2012. Do fault slip data inversions actually yield 'paleostresses' that can be compared with contemporary stresses? A critical discussion. C. R. Geosci. 344, 159–173.

Lagabrielle, Y., Goddéris, Y., Donnadieu, Y., Malavieille, J., and Suarez, M., 2009. The tectonic history of Drake Passage and its possible impacts on global climate. Earth and Planetary Science Letters, 279(3), 197-211.

Lagabrielle, Y., Suárez, M., Malavieille, J., Morata, D., Espinoza, F., Maury, R., Scalabrino, B., Barbero, L., De La Cruz, R., Rossello, E., and Bellon, H., 2007. Pliocene extensional tectonics in Eastern Central Patagonian Cordillera: geochronological constraints and new field evidence. Terra Nova, 19, 413–424.

Lagabrielle, Y., Suárez, M., Rossello, E. A., Hérail, G., Martinod, J., Régnier, M. and De la Cruz., R., 2004. Neogene to Quaternary evolution of the Patagonian Andes at the latitude of the Chile Triple Junction, Tectonophysics, 385, 211 – 241.

Likerman, L., Burlando, J.F., Cristallini, E.O. and Ghiglione, M.C., 2013. Along-strike structural variations in the Southern Patagonian Andes: insights from physical modeling. Tectonophysics, 590, 106–120.

Lonsdale, P., 2005. Creation of the Cocos and Nazca plates by fission of the Farallon plate. Tectonophysics, 404(3), 237-264.

Riedel, W., 1929. Zur mechanik geologischer brucherscheinungen. Zentralblatt für Mineralogie, Geologie und Paläontologie B, 354-368.

Riller, U., Clark, MD., Daxberger, H., Doman, D., Lenauer, I., Plath, S., Santimano, T., 2017. Fault-slip inversions: Their importance in terms of strain, heterogeneity, and kinematics of brittle deformation. J. Struct. Geol. 101, 80-95.

Ritz, JF., Taboada A. (1993). Revolution stress ellipsoids in brittle tectonics resulting from an uncritical use of inverse methods. Bulletin de la Société géologique de France 164 (4), 519-531.

Ronda, G., Ghiglione, M. C., and Barberón, V., 2014. Sistemas de Riedel como mecanismo de deformación en los Andes Patagónicos, norte de Santa Cruz. Actas XIX Congreso Geológico Argentino. Córdoba.

Rosenau, M., Melnick, D., and Echtler, H., 2006. Kinematic constraints on intra-arc shear and strain partitioning in the southern Andes between 38°S and 42°S latitude. Tectonics, 25(4).

Sruoga, P., Japas, M. S., Salani, F. M., & Kleiman, L. E. (2014). La Peligrosa caldera (47 15′ S, 71 40′ W): a key event during the Jurassic ignimbrite flare-up in Southern Patagonia, Argentina. Journal of Volcanology and Geothermal Research, 269, 44-56.

Scalabrino, B., Ritz, J. F., and Lagabrielle, Y., 2011. Relief inversion triggered by subduction of an active spreading ridge: evidence from glacial morphology in Central Patagonia. Terra Nova, 23(2), 63-69.

Scalabrino, B., Lagabrielle, Y., Malavieille, J., Dominguez, S., Melnick, D., Espinoza, F. and Rossello, E., 2010. A morphotectonic analysis of central Patagonian Cordillera: Negative inversion of the Andean belt over a buried spreading center?. Tectonics, 29(2).

Scalabrino, B., Lagabrielle, Y., De la Rupelle, A., Malavieille, J., Polvé, M., Espinoza, F., and Suarez, M., 2009. Subduction of an active spreading ridge beneath southern South America: A review of the Cenozoic geological records from the Andean foreland, central Patagonia (46–47 S). In Subduction Zone Geodynamics (pp. 227-246). Springer, Berlin, Heidelberg.

Somoza, R. and Ghidella, M. E., 2012. Late Cretaceous to recent plate motions in western South America revisited. Earth and Planetary Science Letters, 331, 152-163.

Somoza, R. and Ghidella, M. E., 2005. Convergencia en el margen occidental de América del Sur durante el Cenozoico: subducción de las placas de Nazca, Farallón y Aluk. Revista de la Asociación Geológica Argentina, 60(4), 797-809.

Tavani, S., Storti, F., Lacombe, O., Corradetti, A., Muñoz, J. A., & Mazzoli, S. (2015). A review of deformation pattern templates in foreland basin systems and fold-and-thrust belts: Implications for the state of stress in the frontal regions of thrust wedges. Earth-Science Reviews, 141, 82-104.

Thomson, S.N., Herve, F. and Stockhert, B., 2001. The Mesozoic-Cenozoic denudation history of the Patagonian Andes (southern Chile) and its correlation to diferent subduction processes. Tectonics 20:693–711.

Thomson, S.N., Brandon, M.T., Reiners, P.W., Tomkin, J.H., Vásquez, C. and Wilson, N.J., 2010. Glaciation as a destructive and constructive control on mountain building. Nature 467:313–317.

Tricart P, Lardeaux JM, Schwartz S, Sue C (2006) The late extension in the inner western Alps: a synthesis along the south-Pelvoux transect. Bull Soc Geol Fr 177:299–310

Twiss, R.J. and Unruh, J.R., 1998. Analysis of fault slip inversion: do they constrain stress or strain rate? J. Geophys. Res. 103, 12205–12222.

Wallace, R., 1951. Geometry of shearing stress and relation to faulting. J. Geol. 59, 118–130.

Yamaji, A., 2000. The multiple inverse method: a new technique to separate stresses from heterogeneous fault-slip data. J. Struct. Geol. 22, 441–452.

Yamaji, A., Sato, K. and Otsubo, M., 2011. Multiple Inverse Method Software Package. User´s guide, 1-37.

Figures captions

Figure 1 a) Location of main morphostructural units and tectonic features discussed in the text and location of figures, after Ghiglione *et al*. (2010, 2016) and references therein. Yellow Myr ages in the Pacific trench indicate the time of collision of each Chile ridge segment between oceanic transform fault zones. Red opposing arrows indicate relative convergence between plates cited along the text. COR: Chile oceanic ridge; FZ transform fault zone; LAr Lago Argentino; LBe Lago Belgrano; LPo Lago Posadas; LSM Lago San Martín; LVi Lago Viedma; MEs Magallanes Strait; MFF: Magallanes-Fagnano fault; NSR North Scotia Ridge; RTu Río Turbio; SAz Seno Almirantazgo; UEs Última Esperanza. (b–d) Sketches showing Cenozoic tectonic evolution. Plate configuration and convergence rates from Cande and Leslie (1986), Somoza and Ghidella (2012) and Eagles and Jokat (2014): (b) Late Miocene ~15–10 Ma: Compressional deformation was active along the Basement thrust front. (c) Early Miocene ~20 Ma: the Nazca plate initiates an orthogonal convergence to the South American plate with extensional axes trending ~E–W. d) Eocene ~45 Ma: the Farallon plate's movement is oblique to the trench, leading to major transcurrent mode of deformation.

Figure 2 (a) Geological and structural map modified after Giacosa and Franchi (2001), Escosteguy *et al*. (2003) showing measurement sites and main structures discussed in the text and (b) regional cross-section. See Figure 1 for location of both figures.

Figure 3 (a) Satellite image interpretation of structural lineaments corresponding to large-scale brittle features measured in Jurassic rocks from El Quemado Complex and main mapped thrusts. See geological map from Figure 2 for location. (b) Plot of the 4500 lineaments drawn on the satellite image (Ronda *et al.,* 2014) and the 308 micro-to-meso-

scale fault planes measured on the same sector in this study. (c) Theoretical dextral N–S Riedel system oriented in a fashion where each one of its constituents fits the established directional distribution of fault planes corresponding to the correspondent movement shown in: (d) Fault plane separation according to deformation type, notice the close similarity of those predicted by a Riedel system, shown in (c).

Figure 4 (a) Positive flower structure with left-lateral strike-slip movement in Palaeozoic rocks (Río Lácteo Formation). (b) Detail of the pop-up structure and (c) of the sinistral fault plane. (d–f) Fault plane and sinistral striae near the same site. (g) Stereonets for Site 24, MIM on the left (σ_1 169º and σ_3 76º, n=12, PHI=0,76), and PBT on the right (σ_1 182º and σ_3 88º, n=12, PHI=0,33) along with their misfits.

Figura 5 (a) Photographic panoramas at different zooms with structural interpretation in sedimentary sequences from Lower Miocene (Río Jeinemeni Formation) cropping out at Río Lincoln showing extensional growth strata, probably related to listric faults dipping to the ~W–NW. Synextensional features include increasing thickness of strata towards the faults, decrease in dip from older to younger strata and abrupt thickness changes. (b) Extensional tensor obtained from deformed equivalent sequences in the opposite shore of the river (site 48; see Table 1), with subhorizontal σ_3 best axis at 240°/12° (azimuth/plunge convention) after rotation according to S0 stratification (see Table 1). Concerning this specific tensor, part of the measurements (see supplementary data) may correspond to layer-parallel shortening (LPS, Tavani *et al*., 2015); they have been discarded from the inversion. c) Evolutionary sketch based on cross-cutting relations and synsedimentary deformation for the same site and at Jeinemeni river (see Figure 6). See location in Figure 2.

Figure 6 Photographic panoramas looking to the NW of Jeinemeni river exposures showing superposition of extensional and compressional deformational structures during deposition of the Río Jeinemeni Formation (lower Miocene). The subhorizontal, post-deformation strata belong to the Cerro Boleadoras Formation.

Figure 7 Palaeostress direction map for the MIM method plotted against the geological background. See geological references and site numbers in Figure 1. Additional deformational axes in blue are from Lagabrielle *et al.* (2004) in the northern sector and Diraison *et al.* (2000) south of 47°S.

Figure 8 Φ-ratio (shape of the stress ellipsoid) histograms for all tensors (54 data), broken down by tensor type; see text for discussion.

Table 1 Parameters of the 54 palaeostress tensors including: the site ID number; its coordinates latitude and longitude; the lithology; the orientation of the stratification of the sedimentary bed (S_0), if applicable, *i.e.* not in metasedimentary schists where we indicated "NA" for "non applicable"; the age of the rocks (Pz, Palaeozoic, J, Jurassic, K, Cretaceous, M, Miocene; the name of the regional formation (Fm); the number of all faults and striae measured (N); the number of faults and striae used for each method (n); the orientation (azimuth/plunge) of the computed σ_1 and σ_3 stress axes together with the corresponding ϕ ratio [$\phi = (\sigma_2-\sigma_3)/(\sigma_1-\sigma_3)$]; the average misfit angle (M); the quality parameter assigned to each tensor Q (1: very good, 2: good, 3: poorly constrained), the star indicates the single back-tilted tensor (see text for details); and the deformation mode (DEF), *i.e.* SS for strike-slip, N for normal faulting, and R for reverse faulting. MIM© software (Multiple Inverse

Method version 6.02) was used to determine the stress axes, because of its up-to-date computing strategy (Yamaji *et al.,* 2011).

Supplementary material

A/ Stereonets of the 54 palaeostress tensors are presented following the MIM software representation (equal area projection, lower hemisphere). Each stereonet shows the fault planes and striae used for the computation analysis. The triangles and stars represent σ_1 and σ_3 axes respectively.

B/ table of the 1000 single fault measurements used in this study

TABLE 1

Outcrop parameters								Multiple inverse method						
ID	Latitude	Longitude	Lithology	So_(az/dip)	Age	Fm	N	n	σ1_(az/pl)	σ3_(az/pl)	φ	M	Q	DEF
Site 1-1	46°49,064'	71°50,522'	Tuff	105/15	Ki	RT	11	11	221/6	111,1/1,1	0,6	9,75	2	SS
Site 1-2	46°49,064'	71°50,522'	Tuff	105/15	Ki	RT	27	27	5/80	273,1/0,3	0,74	9,67	1	N
Site 2	46°53,152'	71°53,242'	Andesite	345/40	J	QC	20	17	46/2	251,6/87,7	0,62	10,94	2	R
Site 3	46°57,674'	71°53,698'	Dike	345/40	J	QC	15	11	230,4/5,7	347,4/77,6	0,15	22	3	R
Site 4	47°07,330'	71°50,922'	Tuff	10/30	J	QC	14	12	283,5/5,5	159,2/80,4	0,67	16,4	2	R
Site 5	47°09,090'	71°49,714'	Tuff	180/5	J	QC	17	15	130,7/76,4	260,8/8,8	0,7	7,3	2	N
Site 6	47°09,256'	71°49,661'	Tuff	190/10	J	QC	10	10	79/13	345,6/14,6	0,5	14,22	2	SS
Site 7-1	47°09,702'	71°50,602'	Rhyolite	155/25	J	QC	17	13	134,6/70,9	344/16,7	0,4	8,12	2	N
Site 7-2	47°09,702'	71°50,602'	Rhyolite	155/25	J	QC	21	18	221/2	130,3/19	0,5	27,1	3	SS
Site 8	47°11,137'	71°48,574'	Pyroclastic	135/20	J	QC	26	20	220/8	128,9/8	0,39	19,29	2	SS
Site 9	47°11,743'	71°35,941'	Rhyolite	200/10	J	QC	12	12	102,3/15,8	12,3/0	0,5	8,83	3	SS
Site 10	47°11,445'	71°38,453'	Rhyolite	5/5	J	QC	12	12	123/14	30/11,7	0,52	8,46	2	SS
Site 11	47°13,629'	71°40,279'	Rhyolite	220/15	J	QC	10	10	67/5	158,8/18,9	0,5	9,76	1	SS
Site 12	47°14,093'	71°41,767'	Pyroclastic	225/10	J	QC	14	10	137,7/13,9	229,2/6,1	0,7	15,79	2	SS
Site 13	47°15,701'	71°44,720'	Pyroclastic	10/15	J	QC	17	17	29/7	121,8/20,9	0,5	10,45	2	SS
Site 14	47°19,570'	71°46,385'	Silicified tuff	15/10	J	QC	26	20	334,7/18,3	70,3/16,1	0,45	22,92	2	SS
Site 15-a	47°22,921'	71°43,392'	Silicified tuff	340/13	J	QC	15	10	236/87	9/2	0,2	10,97	2	N
Site 15-b	47°22,921'	71°43,392'	Silicified tuff	340/13	J	QC	13	11	161/8	70,1/6,9	0,21	27,34	3	SS
Site 16	47°27,425'	71°42,368'	Tuff	160/22	J	QC	14	10	175/12	267/18,7	0,58	7,29	1	SS

Site 17	47°30,063'	71°46,186'	Green tuff	35/17	J	QC	21	16	290/12	28/12,6	0,6	20,94	2	SS
Site 18	47°28,758'	71°46,929'	Gray tuff	0/0	J	QC	17	16	283/76	66,2/11,2	0,25	13,06	2	N
Site 19	47°23,748'	71°48,498'	Red tuff	10/19	J	QC	12	11	198/20	291,7/10,3	0,57	15,78	3	SS
Site 20-a	47°21,362'	71°47,664'	Light green tuff	135/22	J	QC	8	8	10/77	244,7/7,6	0,17	12,31	3	N
Site 20-b	47°21,362'	71°47,664'	Light green tuff	135/22	J	QC	16	16	289/8,7	199,1/0,1	0,52	15,56	2	SS
Site 21	47°30,565'	71°56,646'	Pyroclastic	200/64	J	QC	29	22	34,4/11	124,6/1	0,7	25	2	SS
Site 22	47°21,567'	71°58,980'	Quartz sandstones	237/32	Ki	Sp	20	15	342,2/19	248,2/11,2	0,4	20	2	SS
Site 23-a	47°21,211'	71°59,042'	Metasedimentary	NA	Pz	RL	10	10	152,9/18,2	248,4/16,5	0,8	19,64	3	SS
Site 23-b	47°21,211'	71°59,042'	Rhyolite sill	160/40	J	QC	9	9	267/17	173,8/10,6	0,41	16,13	2	SS
Site 24	47°26,398'	72°04,122'	Metasedimentary	NA	Pz	RL	14	12	169/12	76,3/12,7	0,76	21,43	3	SS
Site 25	47°25,760'	72°01,747'	Metasedimentary	NA	Pz	RL	18	14	145/19,6	319,1/70,4	0,6	18,88	2	R
Site 26-a	47°25,164'	71°58,496'	Rhyolitic tuff	170/50	J	QC	10	10	354,8/9,4	87,5/15,7	0,52	12,69	2	SS
Site 26-b	47°25,164'	71°58,496'	Rhyolitic tuff	170/50	J	QC	12	11	110/16	200,5/2	0,51	13,94	2	SS
Site 27	47°25,130'	71°57,822'	Sandstones	290/36	Ki	RB	23	15	276/77	69,4/11,8	0,75	16,19	2	N
Site 28	47°44,132'	72°05,674'	Conglomerates	330/30	J	QC	21	17	262/8	170,2/11,9	0,11	15,4	2	SS
Site 29	47°43,954'	72°05,515'	Pyroclastic	340/45	J	QC	40	33	111/17,7	203,7/12,7	0,9	29,72	3	SS
Site 30	47°43,729'	72°05,251'	White tuff	350/16	J	QC	25	21	18,4/84,9	194,4/5,1	0,2	16,55	2	N
Site 31	47°46,328'	72°11,933'	Metasedimentary	NA	Pz	RL	14	10	193,4/77,6	20,5/12,3	0,2	21,96	3	N
Site 32	47°45,954'	72°09,192'	Metasedimentary	NA	Pz	RL	12	9	133,7/19,1	36,9/18,9	0,7	18,47	2	SS
Site 33	47°47,187'	72°02,999'	Pyroclastic	355/23	J	QC	19	15	40/1	130,1/9,9	0,75	10,73	3	SS
Site 34	47º49,820'	72º8,716'	Metasedimentary	NA	Pz	RL	22	18	51/84	261,2/5,2	0,37	15,37	2	N
Site 35	47°50,079'	72°05,197'	Tuff	190/41	J	QC	21	21	112/5	20,5/16,9	0,1	16,7	1	SS
Site 36	47°47,877'	72°00,334'	Sandstones	350/25	Ki	RB	8	8	100/13	194,1/17,5	0,25	14,25	3	SS

Site 37	47°51,032'	72°05,521'	Tuff	180/18	J	QC	19	18	354/10	260,5/18,7	0,85	17,13	3	SS
Site 38	47°50,967'	72°05,992'	Green tuff	185/24	J	QC	18	14	112/71	280,4/18,7	0,74	22,31	2	N
Site 39	47°53,599'	72°05,598'	Dark Green Tuff	350/15	J	QC	30	25	276,6/75,8	142/10	0,6	15,52	2	N
Site 40	47°56,899'	72°07,378'	Green dacite	355/32	J	QC	20	19	44,1/82,2	149/1,9	0,5	16,63	2	N
Site 41	47°57,099'	72°09,757'	Silicified tuff	350/28	J	QC	20	17	282/10	189,9/11,9	0,7	26,9	3	SS
Site 42	47°33,955'	71°54,090'	Sandstones	0/0	Mi	SC	25	24	270,8/10,7	180,3/3	0,3	9,4	1	SS
Site 43	47°03,956'	70°49,184'	Sandstones	0/0	Mi	SC	20	19	50,9/86,3	310,9/0,7	0,3	12,94	1	N
Site 44	46°36,435'	71°31,749'	Sandstones	30/5	Mi	SC	20	14	26,6/79,1	190/10,4	0,2	12,01	2	N
Site 45	46°44,312'	71°43,328'	Sandstones	5/5	Mi	SC	12	9	297,3/83,3	27,2/0	0,2	7,83	2	N
Site 46	46°42,078'	71°38,763'	Sandstones	0/0	Mi	SC	17	14	321,2/80,5	151,3/9,4	0,2	7,9	1	N
Site 47	46°38,324'	71°38,685'	Sandstones	350/5	Mi	Cnt	16	10	333,2/72,4	140,2/17,2	0,65	8,84	2	N
Site 48	46°53,158'	71°52,353'	Sandstones	340/86	Mi	Jn	33	21	78,5/77,3	240,2/12,1	0,5	13,7	2*	N

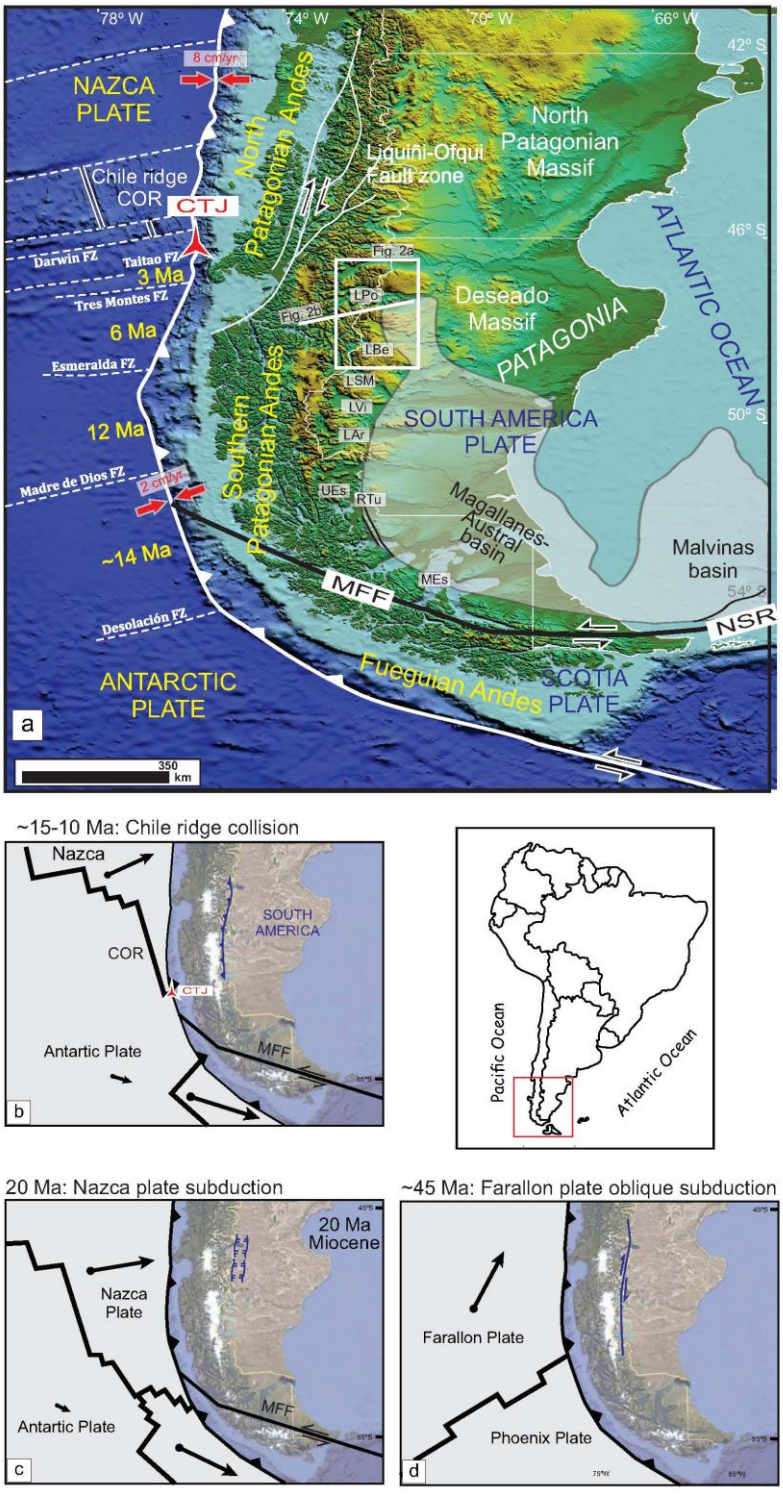

FIGURE 1

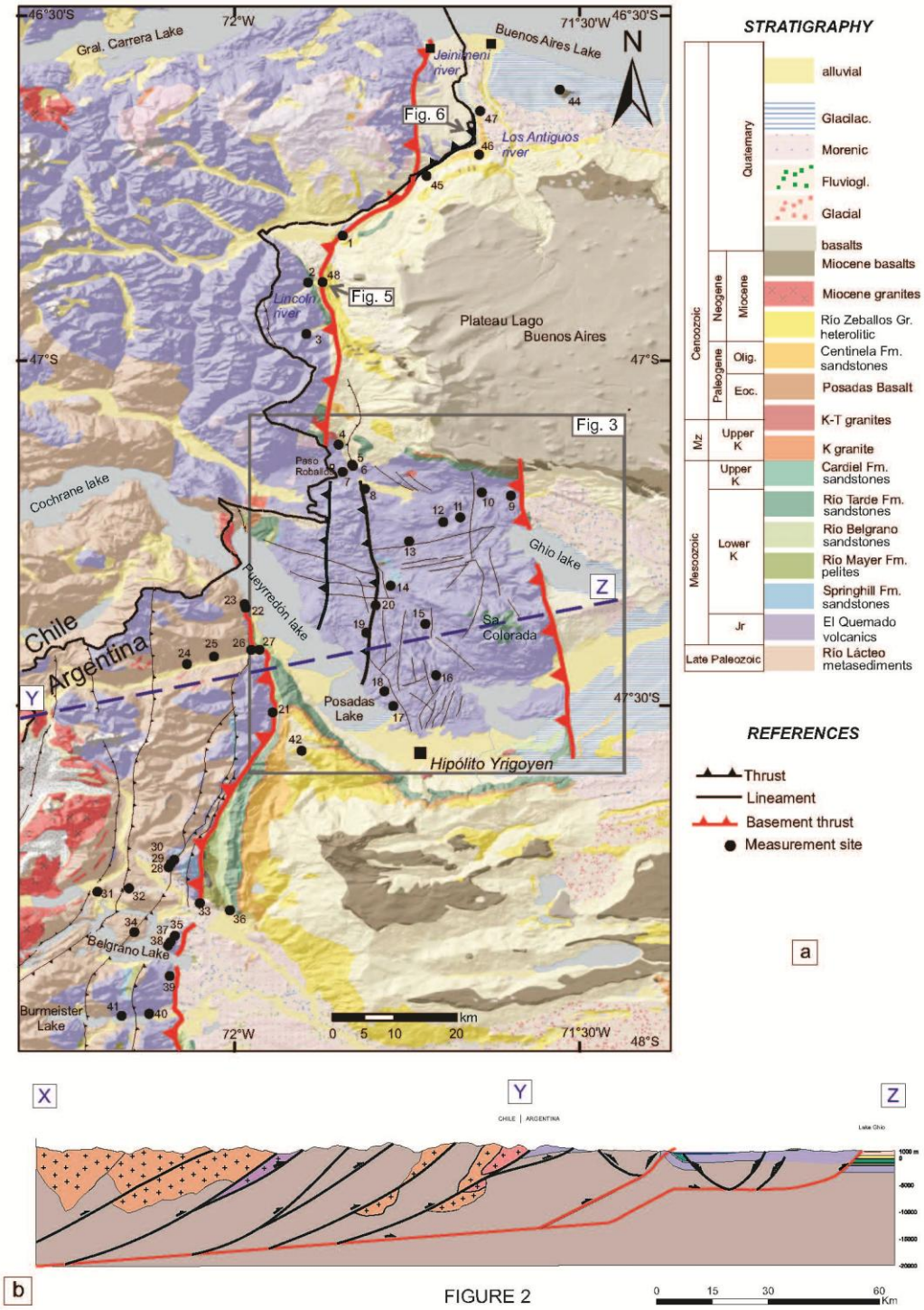

FIGURE 2

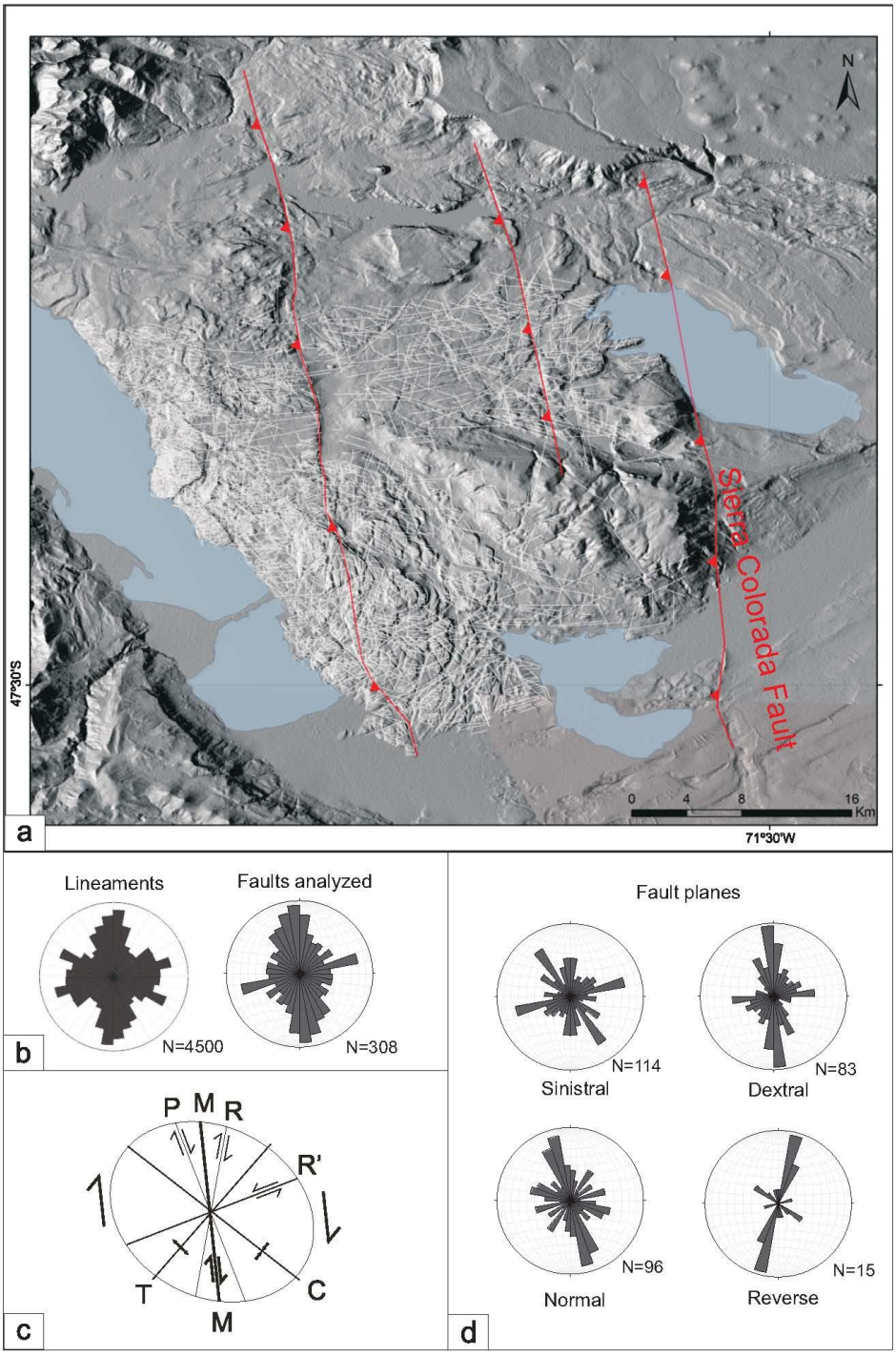

FIGURE 3

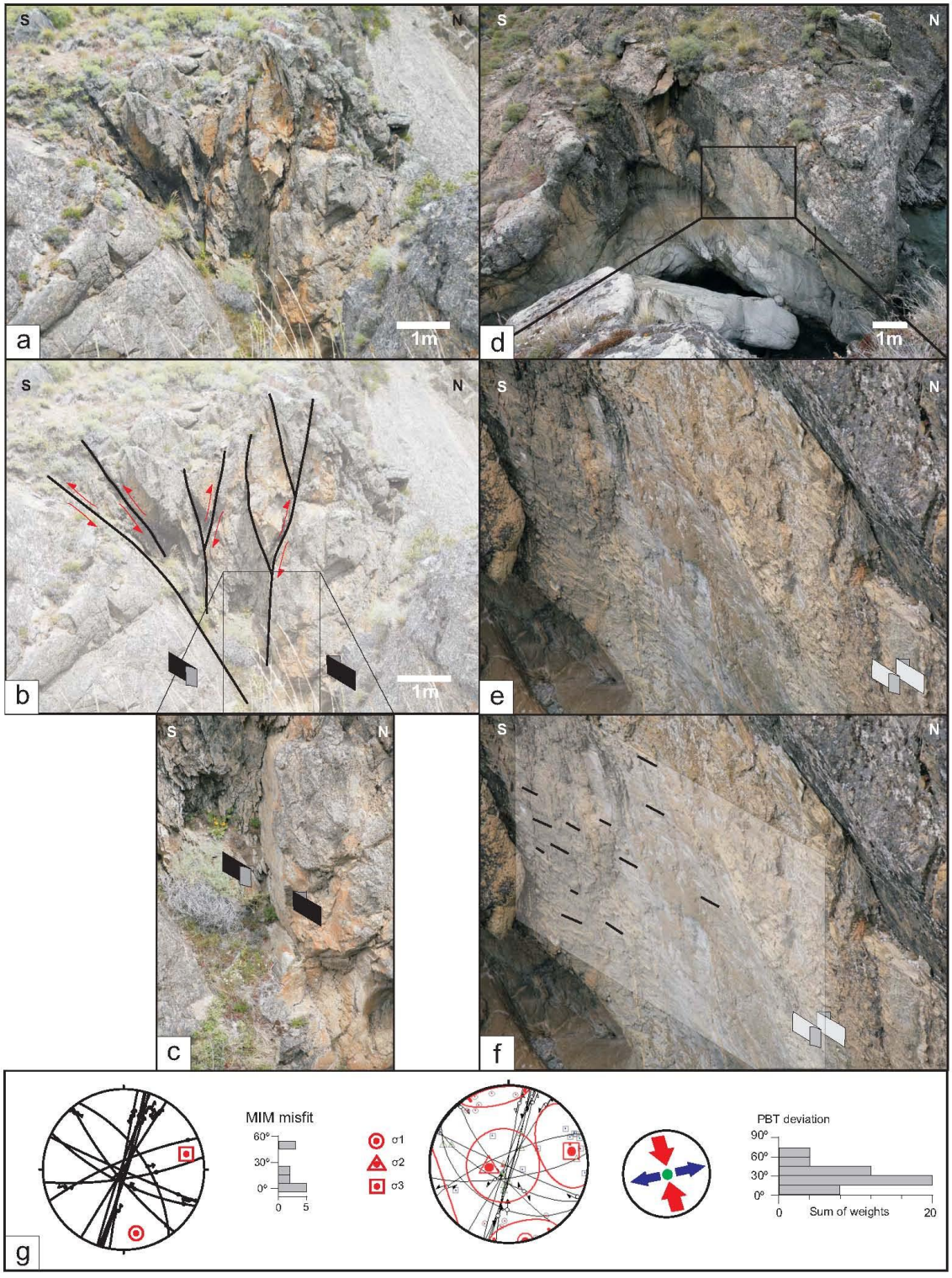

FIGURE 4

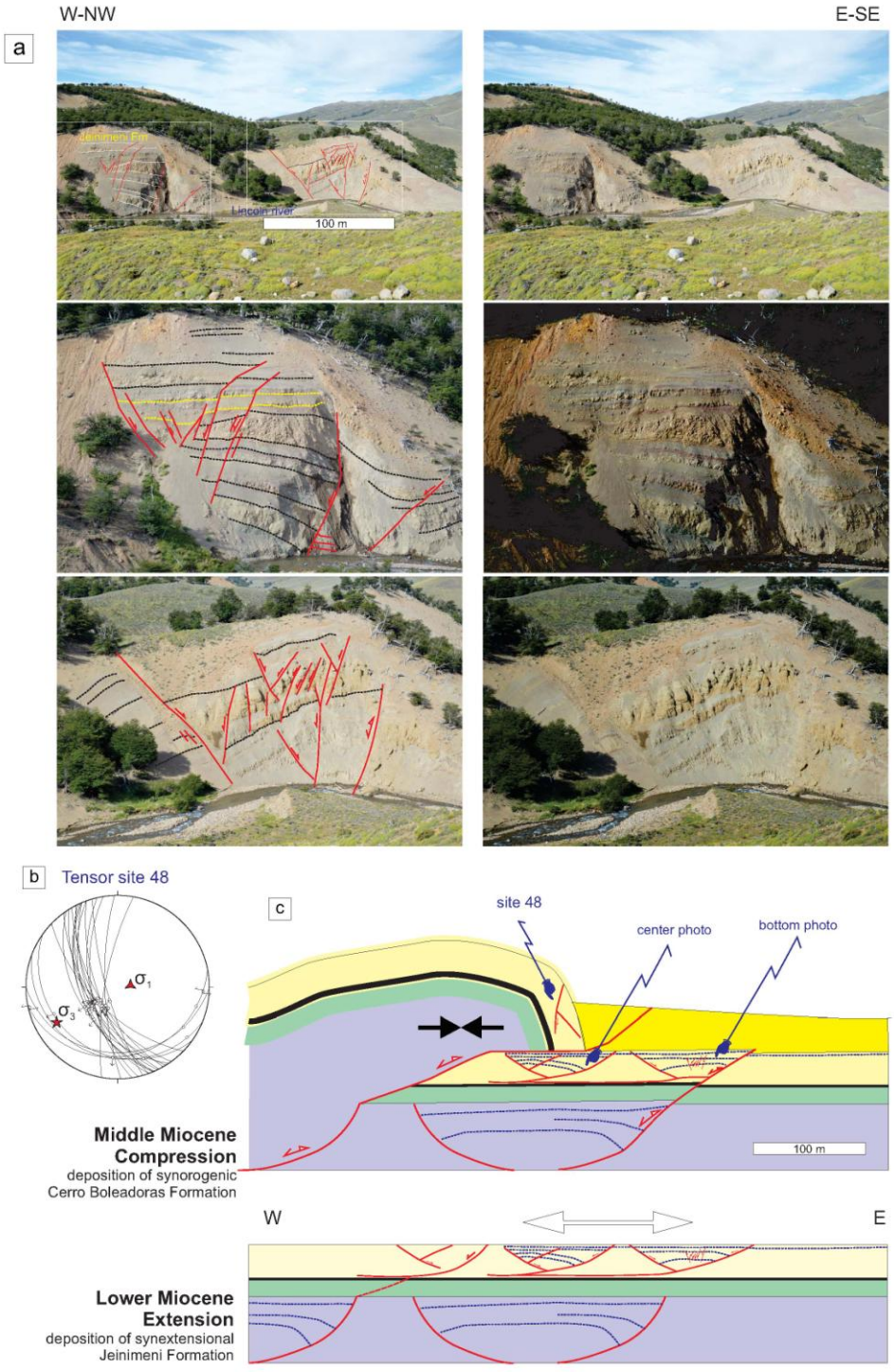

FIGURE 5

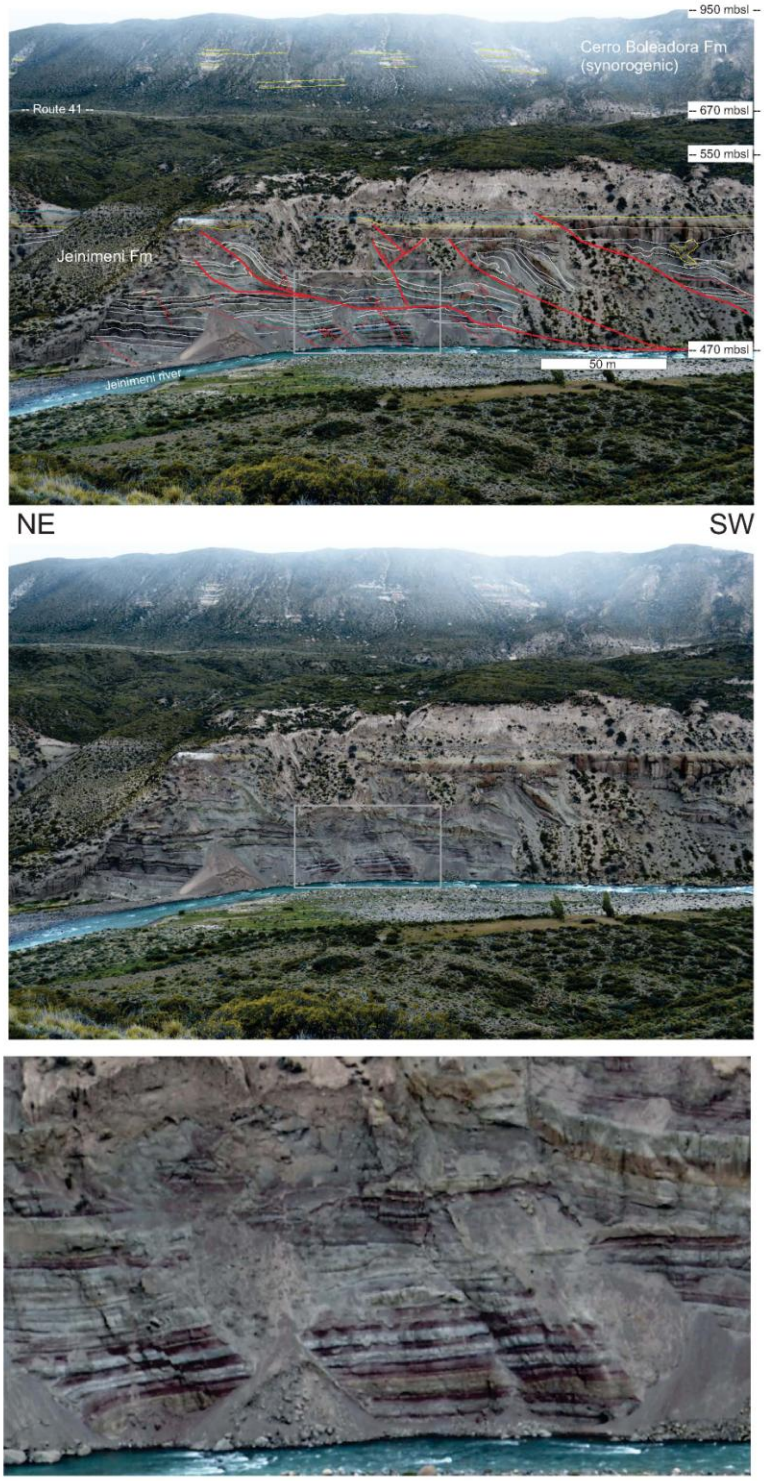

FIGURE 6

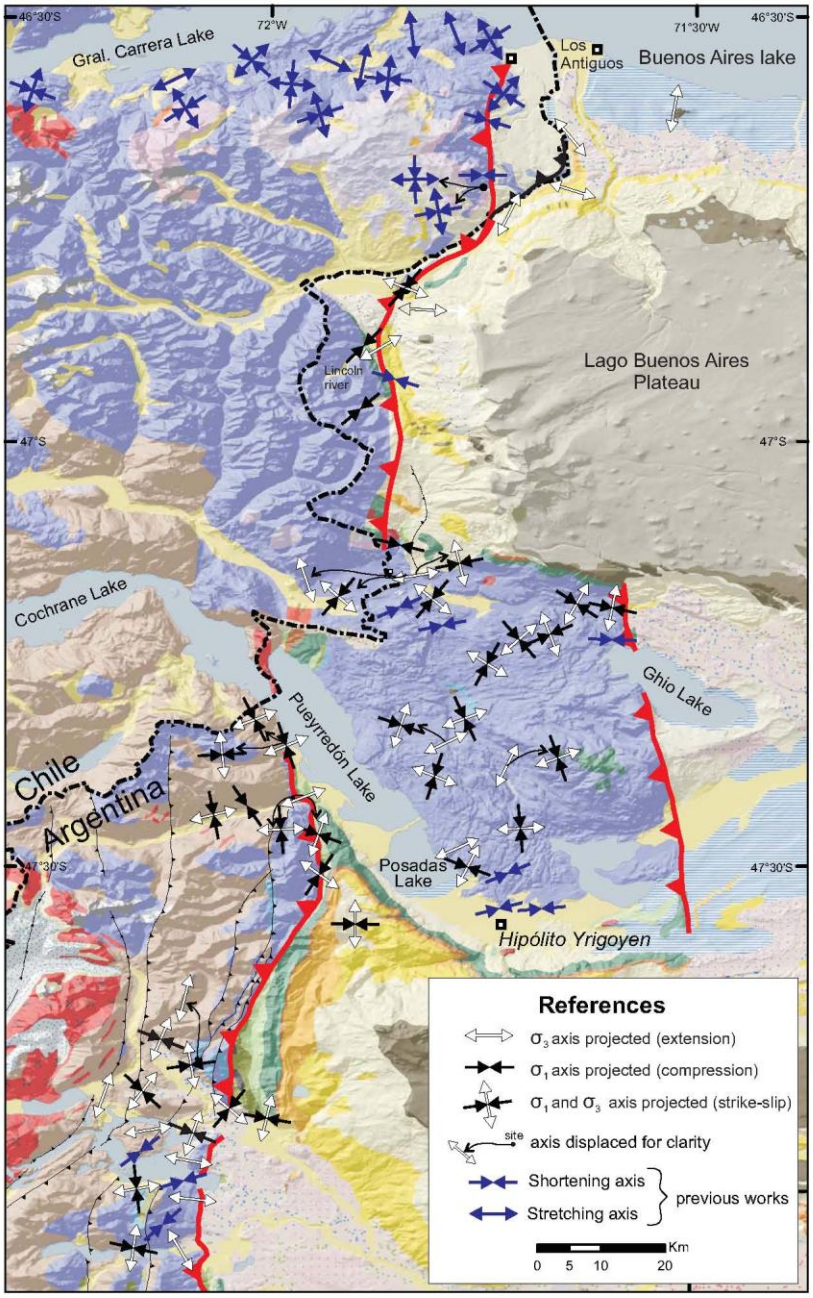

FIGURE 7

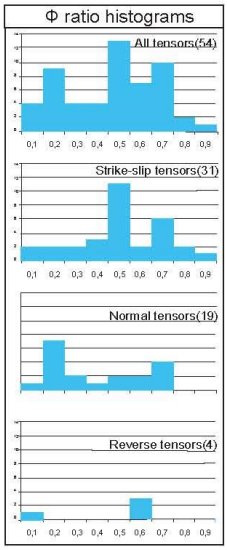

FIGURE 8